Mechanosensing is critical for axon growth in the developing brain

David E Koser[1,4,8], Amelia J Thompson[1,8], Sarah K Foster[1,8], Asha Dwivedy[1,8], Eva K Pillai[1], Graham K Sheridan[1,5], Hanno Svoboda[1,6], Matheus Viana[2], Luciano da F Costa[2], Jochen Guck[3,7], Christine E Holt[1] & Kristian Franze[1,3]

1Department of Physiology, Development and Neuroscience, University of Cambridge, Cambridge, UK. 2São Carlos Institute of Physics, University of São Paulo, São Carlos, Brazil. 3Department of Physics, Cavendish Laboratory, University of Cambridge, Cambridge, UK. 4Present addresses: Department of Clinical Neurobiology, Medical Faculty of Heidelberg University and German Cancer Research Center (DKFZ), Heidelberg, Germany. 5Present address: School of Pharmacy and Biomolecular Sciences, University of Brighton, Brighton, UK. 6Present address: Roche Innovation Center Basel, Basel, Switzerland. 7Present address: Biotechnology Center, Technische Universität Dresden, Dresden, Germany. 8These authors contributed equally to this work. Correspondence should be addressed to K.F. (kf284@cam.ac.uk).

During nervous system development, neurons extend axons along well-defined pathways. The current understanding of axon pathfinding is based mainly on chemical signaling. However, growing neurons interact not only chemically but also mechanically with their environment. Here we identify mechanical signals as important regulators of axon pathfinding. *In vitro*, substrate stiffness determined growth patterns of *Xenopus* retinal ganglion cell axons. *In vivo* atomic force microscopy revealed a noticeable pattern of stiffness gradients in the embryonic brain. Retinal ganglion cell axons grew toward softer tissue, which was reproduced *in vitro* in the absence of chemical gradients. To test the importance of mechanical signals for axon growth *in vivo*, we altered brain stiffness, blocked mechanotransduction pharmacologically and knocked down the mechanosensitive ion channel piezo1. All treatments resulted in aberrant axonal growth and pathfinding errors, suggesting that local tissue stiffness, read out by mechanosensitive ion channels, is critically involved in instructing neuronal growth *in vivo*.

During the development of the CNS, each neuron extends an axon, which is the dominant cell process, and a number of finer, branched dendrites. Before connecting with their targets, axons grow along well-defined pathways in a stereotypic manner. Since the introduction of Sperry's chemoaffinity hypothesis more than 50 years ago[1], it has generally been accepted that axon guidance is regulated primarily by chemical signals[2,3].

In the developing *Xenopus laevis* optic pathway, which is one of the best understood model systems of axon pathfinding, retinal ganglion cell (RGC) axons leave the retina via the optic nerve, cross the midline at the optic chiasm, grow along the contralateral brain surface in the optic tract (OT) and terminate in the optic tectum. Axon guidance along the OT, and particularly the caudal turn of axons in the mid-diencephalon, is thought to be mainly controlled by the repellent chemical cues slit1, slit2 and semaphorin 3A[4–6], which are expressed in the telencephalon and diencephalon.

Growth implies motion, however, and motion is driven by forces. Growing axons must exert forces on their environment and interact with it not only chemically but also mechanically[7–10]. Neuronal growth may thus be influenced by the mechanical properties of the environment, as originally shown *in vitro*[11]. Recent work has revealed that, *in vitro*, neuronal growth patterns, neurite extension, branching patterns and neuronal traction forces all change with substrate stiffness[10,12–16]. Since CNS tissue is mechanically heterogeneous[17–23], growing axons are likely to encounter tissue regions with different mechanical properties. While

local tissue mechanics might thus provide important signals to growing axons, the mechanical properties of developing CNS tissue *in vivo* are currently unknown, and the potential neuronal response to mechanical signals *in vivo* is poorly understood.

Here, we used *in vitro* mechanosensitivity assays, *in vivo* atomic force microscopy (AFM) and perturbations of both brain tissue stiffness and neuronal mechanosensitivity to investigate how mechanical signals affect neuronal growth. We found that axonal growth patterns depend strongly on the local mechanical properties of the surrounding tissue, suggesting that, *in vivo*, growing neurons respond not only to chemical but also to mechanical signals.

RESULTS

RGC axons are mechanosensitive

To investigate *Xenopus* RGC axon mechanosensitivity, we first cultured eye primordia, which contain intact retinae from which RGCs extend their axons, on polyacrylamide substrates of controlled stiffness24. We used two different substrates to probe axonal mechanosensitivity: 'stiff' substrates with a shear modulus of 1 kPa and 'soft' substrates with a shear modulus of 0.1 kPa, which correspond approximately to the upper and lower bounds of brain tissue stiffness, respectively25. The substrates were coated with laminin, the density of which was independent of substrate stiffness (**Supplementary Fig. 1c**). Thus cells cultured on soft and stiff substrates were only exposed to different mechanical signals, while their chemical environments were similar.

After 24 h, axons grown on stiff substrates were significantly longer than those grown on soft substrates, as assessed by Sholl analysis ($P < 10-6$, one-way ANOVA followed by Bonferroni *post hoc* test; **Fig. 1a**,**b**,**d**,**e**). RGCs cultured on substrates coated with fibronectin, which engages different integrins than laminin26, also grew significantly longer axons on stiff substrates ($P < 10-5$, two-tailed *t*-test; **Supplementary Fig. 2a**–**d**), suggesting that neurons were mechanosensitive irrespective of the type of integrins involved in cell adhesion.

In agreement with the Sholl analysis, time-lapse movies revealed that the average extension velocity of axons, i.e., the average distance between the proximal and distal ends of the axon per time interval, was significantly higher on stiff than on soft substrates (median velocities of 35.0 μm/h versus 22.6 μm/h; $P < 10-5$, Mann-Whitney test; **Fig. 1g** and **Supplementary Movies 1** and **2**). However, when we assessed the absolute distance growth cones, which are the tips of advancing axons, moved in a given time, we found that they actually moved faster and explored their environment more on soft substrates than on stiff substrates (109 ± 3 μm/h versus 99 ± 2 μm/h; $P < 0.01$, two-tailed *t*-test; **Fig. 1h**). Thus the directionality of axonal growth, which is defined as the ratio between axon extension and the length of the path covered by the growth cone, was significantly reduced on soft substrates ($P < 10-6$; **Fig. 1i**), indicating that axon growth is more directionally persistent on stiffer substrates.

The more explorative motion of growth cones on soft substrates was reflected in the appearance of the explant cultures. While on stiff substrates axons grew rather straight and parallel to each other (i.e., formed bundles), on soft substrates axons grew less coherently, crossed each other more frequently and appeared to splay apart (**Fig. 1j** and **Supplementary Fig. 2e**–**g**). Together, these experiments showed that, *in vitro*, growing *Xenopus* RGC axons respond to mechanical signals.

Mechanosensing is mediated by stretch-activated ion channels

Previous *in vitro* experiments have suggested an involvement of stretch-activated ion channels in neuronal mechanosensitivity27–30. As the opening probability of mechanosensitive ion channels increases on stiffer substrates27–29,31, impeding the channels' activity should prevent neurons from detecting 'stiff' and result in the equivalent of a 'soft' phenotype.

Piezo1, which forms a mechanically activated cation channel32,33, has been identified as a key player in several mechanotransduction cascades in developing systems31,34,35. Using immunocytochemistry, we found a positive signal for piezo1 distributed in punctate patterns all along axons and in growth cones of

Xenopus RGCs (**Fig. 1f**). We then applied the spider venom peptide GsMTx4, which blocks the activity of mechanosensitive ion channels including piezo1 (ref. 36), to eye primordia cultures. As predicted, axons grown on stiff substrates and treated with GsMTx4 were significantly shorter than axons in the control group ($P < 10-7$, one-way ANOVA followed by Bonferroni *post hoc* test) and strongly resembled axons grown on soft substrates ($P = 1.00$; **Fig. 1c**–**e**), indicating that mechanosensing of *Xenopus* RGCs is mediated by mechanosensitive ion channels.

Stiffness gradients in developing brain tissue

In order to investigate the mechanical environment RGC axons encounter *in vivo*, we developed an AFM-based approach to map the local tissue stiffness of the exposed intact developing brain at different developmental stages by force-indentation measurements (**Fig. 2a** and Online Methods). Tissue stiffness was quantified by the reduced apparent elastic modulus *K*, where a larger *K* value indicates stiffer tissue. Stiffness maps had spatial resolutions of 20–25 μm, a length scale relevant to individual neuronal growth cones16. RGC axons were visualized using epifluorescence by introducing a fluorescent protein under the control of the Ath5 promotor (Ath5:mGFP), which in the *Xenopus* retina is specific to RGCs37.

AFM measurements were carried out at two different developmental time points: when the first axons had left the optic chiasm and entered the ventral OT (developmental stage 33/34) and again when the first axons had reached the optic tectum (stages 39 and 40; **Fig. 2b**). At both time points, tissue stiffness was heterogeneously distributed (**Fig. 2c**,**d** and **Supplementary Fig. 3a**,**b**). Analysis of the stiffness of distinct tissue regions revealed that, at stage 33/34, the telencephalon and diencephalon and, at stages 39 and 40, the OT, were significantly stiffer than the optic tectum ($P33/34 < 10-8$, $P39\text{-}40 < 10-2$; **Fig. 2f**,**g**). Furthermore, at stages 39 and 40, tissue rostral to the OT was significantly stiffer than that caudal to it ($P < 10-4$; **Fig. 2h**), resulting in a stiffness gradient perpendicular to the growth direction of RGC axons.

In order to determine the structural origin of this stiffness gradient in the brain, we first tested if RGC axons themselves were involved. We ablated eye primordia in early *Xenopus* embryos. Brains of those embryos developed normally, but no RGC axons entered the diencephalon. We found similar stiffness distributions in the telencephalon and diencephalon of these brains as in control brains (**Supplementary Fig. 3c**), suggesting that RGC axons themselves did not cause the observed stiffness gradients.

While the extracellular matrix (ECM) contributes to overall CNS tissue stiffness22,38, mechanical heterogeneities appear to be largely established by the tissue's cellular constituents19,22,23,39. In other CNS tissues, stiffness scales with cell body density22; we therefore used immunohistochemistry to investigate the distribution of cell nuclei in the vicinity of the OT. Nuclei in whole mount brain preparations were labeled using DAPI and the area they occupied in a given region was determined. Cell body densities rostral to the OT were significantly higher than those caudal to it ($P < 10-5$, paired two-tailed *t*-test; **Fig. 2e**,**i**), suggesting a functional connection of the local cell body distribution to the presence and direction of the observed stiffness gradient.

Axons grow toward soft tissue

We found that RGC axons grow perpendicular to a local stiffness gradient in the brain (**Fig. 2d**,**h**). To assess the impact of this stiffness gradient on axon growth, we quantified the local curvature, *C*, of the OT approximately every 40 μm along its length by fitting a circle of radius *R* to the OT as indicated in **Figure 3a** and calculating $C = 1/R$. We then calculated the local stiffness gradient *M* perpendicular to the OT at each position by subtracting the apparent elastic modulus *K* averaged over an area of 100 × 100 μm2 caudal to the

OT from the average *K* rostral to it. This difference in *K* was then divided by 100 μm, resulting in a stiffness gradient *M* expressed in Pa/μm (**Fig. 3a**).

The local curvature *C* of axons at any position along the OT strongly correlated with the tissue's local stiffness gradient *M* at that position. RGC axons encountering stiffness gradients *in vivo* clearly turned away from stiffer and grew toward softer tissue ($P < 10-3$, one-sample Wilcoxon signed-rank test; **Fig. 3b**,**c**). Notably, however, the curvature of the OT was independent of the absolute tissue stiffness (**Supplementary Fig. 4c**).

To test whether mechanical signals imposed by stiffness gradients are instructive rather than just permissive to axon growth, we developed cell culture substrates incorporating stiffness gradients similar to those found *in vivo* (**Supplementary Fig. 1** and Online Methods), which allowed us to reduce the complexity of the neuronal environment and to study the effect of stiffness gradients on axon growth in the absence of chemical guidance cues. To test the correlation between stiffness gradients and axon turning in these *in vitro* assays, eye primordia were cultured on stiffness gradients and imaged, and the orientations of axons were analyzed using two complementary approaches.

We first used time-lapse microscopy to quantify the dynamic turning of individual axon bundles growing perpendicular to the stiffness gradient (with respect to their initial growth direction; **Fig. 3d**,**e**). We verified these results by analyzing the orientation of all axons of an explant (~2,800 segments per eye primordium on average) relative to their original orientation at the end of an experiment (**Fig. 3f**,**g** and Online Methods). Both approaches showed that axon bundles also preferentially turned toward softer regions *in vitro* ($P \leq 0.05$), in the absence of chemical gradients.

Softening of brain tissue leads to aberrant axon growth

As mentioned above, the ECM contributes to overall CNS tissue stiffness (although probably less to mechanical heterogeneities). To test if brain tissue stiffness provides an instructive signal for RGC axon growth *in vivo*, we first perturbed the mechanical properties of developing *Xenopus* brains by manipulating their ECM composition. Chondroitin sulfate (CS) proteoglycans are an abundant ECM component in the developing brain40. After applying CS to exposed brains *in vivo*, we still found similar stiffness gradients in treated brains as in control brains; however, the overall tissue stiffness was significantly decreased ($P < 10-9$, Mann-Whitney test; **Fig. 4a**–**c** and **Supplementary Fig. 3d**), particularly in the region in front of the OT ($P < 10-10$; **Fig. 4c**).

Because the turning of RGC axons toward soft tissue did not depend on absolute brain stiffness but rather on the strength of the local stiffness gradient (**Fig. 3b** and **Supplementary Fig. 4c**), axons still preferentially turned toward softer tissue in CS-treated brains (**Supplementary Fig. 4**). However, in agreement with our *in vitro* experiments and a previous study40, RGC axons in these softened brains dispersed widely from their normal trajectory, with reduced directionality and fasciculation (**Fig. 4d**), thus resembling axon behavior on soft substrates *in vitro* (**Fig. 1**). To quantify OT phenotypes, we fitted ellipses around OTs and compared the ratios between the long and short axes of the ellipses, i.e., their elongation24 (**Fig. 4e**). The elongation of the OT in CS-treated brains was significantly decreased compared to controls ($P < 10-5$, two-tailed *t*-test; **Fig.**

4f), suggesting that different mechanical instructions provided by CS-treated, softened brain tissue likely contributed to RGC axon defasciculation and aberrant growth.

Local mechanical perturbation of brain tissue redirects axons

As CS proteoglycans are likely involved in binding and presenting various trophic and tropic factors to axons40, the OT phenotype observed after increasing the brain's CS content might be due not only to mechanical but also to chemical changes in the tissue. To perturb brain mechanics without altering the chemical environment, we used AFM to apply a sustained compressive force (F) of 30 nN to exposed embryonic brains *in vivo* (**Fig. 4g**) with a spheroidal probe 87 μm in diameter. The resulting mechanical stress, defined as $\sigma = F/A$ = ~30 pN/μm2 = 30 Pa, where A is the contact area, led to a maximum tissue strain of $\varepsilon \propto \sigma/Kmax$ = ~7.5% (corresponding to a maximum indentation of $\delta max = 3.6 \pm 0.2$ μm).

The experiment commenced at stage 35/36, when the fluorescently labeled OT was already visible but had not started to turn caudally in the mid-diencephalon (**Supplementary Fig. 5a**), and finished ~6 h later, when embryos had reached stage 39. The compressive force was applied to the region just caudal to the anticipated OT turn, where the tissue would normally be soft (cf. **Fig. 2d**). Importantly, brain tissue is nonlinearly elastic and stiffens under compression18,21,41 ($P < 0.01$, Kruskal-Wallis ANOVA; **Supplementary Fig. 5h**).

In all experiments, axons avoided growing under the center of the probe, where the compressive strain was largest. While in time-matched control embryos the OT grew normally and frequently formed a caudal bend in the mid-diencephalon (**Fig. 4h**), in two of five experiments axons grew straight, passed the site of indentation laterally, and the OT did not substantially turn (**Supplementary Fig. 5f**,**g**). In the other three cases, RGC axons deviated from their normal path to grow either away from or around the compressed tissue (**Fig. 4i** and **Supplementary Fig. 5b**–**e**). These experiments showed that solely mechanical perturbation of brain tissue is sufficient to alter axon growth patterns.

Mechanosensing via piezo1 is critical for axon growth *in vivo*

The previous set of experiments indicated that RGC axons respond to mechanical signals *in vivo*. To test if their mechanosensitive behavior was mediated by mechanosensitive ion channels, as in our *in vitro* experiments (**Fig. 1**), we either applied GsMTx4 to exposed brains of stage 33/34 embryos (cf. **Fig. 2b**) or downregulated piezo1 expression by ~42% using morpholino knockdown *in vivo* (**Supplementary Fig. 6d**,**e**). Following both manipulations, at stages 39 and 40 RGC axons dispersed widely from their normal trajectory and assumed a phenotype similar to that displayed by axons grown on softer substrates *in vitro* (**Fig. 1**), with directional incoherence, decreased length and overall reduced elongation ($P < 0.01$, two-tailed t-test; **Fig. 5**).

This phenotype was maintained in the piezo1 morpholino-treated animals at stage 42 (**Supplementary Fig. 6a**–**c**), at which point OT growth and tectal innervation are normally complete (~1 d older than those shown in **Fig. 5**), indicating that piezo1 knockdown led to pathfinding abnormalities rather than merely to slowed axon growth. Hence, our experiments suggested that RGC mechanosensitivity, which is involved in controlling axon growth, is mediated by piezo1 *in vivo*.

DISCUSSION

We have shown that, *in vitro* as well as *in vivo*, *Xenopus* RGC axons respond to mechanical signals in their environment (**Fig. 6a**). Tissue stiffness regulates the length of axons and their degree of spreading: axons grow faster, straighter and more parallel on stiffer substrates (**Fig. 1**). A higher stiffness, causing persistent growth and facilitating fasciculation, thus seems favorable for tissues through which axons have to grow. A lower stiffness, on the other hand, promoting slowed exploratory growth and splaying of axons, seems beneficial for regions where axons have to search for their targets and form synapses. Accordingly, tissue in the vicinity of the OT, where axons are tightly bundled, is stiffer than the rostral part of the tectum (**Fig. 2g**), where axons splay apart, branch and form synapses. In line with this observation, spinal cord neurons *in vitro* branch more on softer substrates12.

Furthermore, local stiffness gradients guide RGC axon growth. Non-neuronal cell types responding to stiffness gradients *in vitro* usually migrate toward the stiffer side of their substrate in a process termed durotaxis42. Durotaxis depends mostly on the strength of the gradient and is largely independent of the absolute substrate stiffness43,44, similarly to what we observed in our *in vivo* experiments (**Supplementary Fig. 4c**,**d**). However, in contrast to other cell types, RGC axon bundles turned toward the softer side of their growth substrate, both *in vitro* and *in vivo*. While individual growth cones might possess neuron-specific mechanotransduction mechanisms causing this response27,28, growth of axon bundles toward soft areas could also be at least partly a collective effect (**Fig. 6b**). Growth velocities of axons are higher on stiffer substrates (**Fig. 1g**). When axon bundles grow perpendicular to a stiffness gradient, the faster axons on the stiffer side will be 'pulled' toward the tightly coupled slower axons on the softer side and consequently turn toward them (similarly to phototropism in plants, in which cells on the side of the stem farthest from the light extend more than cells closer to the light).

The mechanical properties of embryonic brain tissue have previously been studied in mice and chickens20,45. While Xu and colleagues suggested that embryonic chick brain is mechanically rather homogeneous and does not change its elastic stiffness over time45, in the mouse embryonic cerebral cortex, tissue stiffness is region-dependent and developmental-stage-dependent20. Both studies were done *ex vivo*. Using an *in vivo* AFM approach, we obtained stiffness maps of intact *Xenopus* brain with a spatial resolution on the order of the size of neuronal growth cones. We found that the stereotypic caudal bend of the OT in the mid-diencephalon coincides with a steep stiffness gradient in the tissue (**Fig. 2** and **Supplementary Fig. 3**). Axons in that region turned away from stiffer tissue as in our *in vitro* experiments, and the curvature of the OT correlated strongly with the strength of the gradient but not with the absolute tissue stiffness (**Fig. 3** and **Supplementary Fig. 4**).

The stiffness gradient likely originates mostly from the change in cell body density from rostral to caudal of the OT. Similarly, in the mouse spinal cord, higher cell densities are associated with larger tissue stiffness22. While RGC axons respond to the mechanical stiffness of their environment (cf. **Fig. 1**), the space available for axons to grow through might contribute an additional mechanical signal controlling axon growth *in vivo*. Higher cell body densities likely also result in a decrease in available space and thus increased steric hindrance, which could add to the mechanotactic growth of RGC axons in the mid-diencephalon toward softer and less dense regions of the brain (cf. **Fig. 2e**).

Similarly, the change in RGC growth direction following the local application of a sustained compressive force to *Xenopus* brains (**Fig. 4**) is likely the result of a combination of three different mechanical signals directly impacting neuronal growth. (i) CNS tissue stiffens under compression18,21,22,41, so the stiffness of the tissue underneath the AFM probe was increased (**Fig. 4g** and **Supplementary Fig. 5h**). Such a change in stiffness can be read out by RGC axons via piezo1 (**Figs. 1** and **5**). Compression of the tissue via a bead should lead to a local gradient in stiffness, with maximum stiffening occurring at the center of the probe where the strain is highest. This induced stiffness gradient might repel axon bundles as described above. (ii) Local tissue compression could additionally lead to a local decrease in the available space, causing RGC axons to avoid and grow around the denser region. (iii) Finally, pushing on the tissue might also directly trigger an immediate mechanosensitive response in neurons27, which at least at short time-scales might contribute to changing growth directions. Moreover, all three mechanisms may potentially impact chemical signaling pathways, thus also indirectly contributing to changing RGC axon growth directions (see below).

Mechanosensitive ion channels open more frequently in neurons grown in stiffer environments27–29,31. Blocking these channels thus prevents neurons from detecting 'stiff' (**Fig. 1c–e**), suggesting a plausible mechanism by which RGC axons in brains treated with GsMTx4 or piezo1 morpholinos were shorter, grew with reduced directionality, and fanned out. It is likely that there are other mechanisms involved in neuronal mechanotransduction25,46; however, interfering with these ion channels alone was sufficient to significantly impact axon growth *in vitro* as well as *in vivo*.

While we cannot rule out the possibility that our treatments also affected other cells in the tissue35, the results of these treatments do indicate that changing either tissue mechanics or the cellular susceptibility to mechanical signals impacts RGC axon growth (**Figs. 4** and **5**). The mechanism by which CS treatment disrupts axon pathfinding in the OT is still poorly understood. It has been speculated that CS might modulate axon pathfinding via CS-binding molecules40. Here we provide an alternative or additional mechanism. The less directionally persistent axonal growth and the breakdown of fasciculation could at least partly be attributed to a softening of the tissue, likely due to increased hydration through the introduction of additional sulfate groups47.

It is possible that interfering with mechanotransduction not only directly but also indirectly altered RGC axon growth. Cells are likely to integrate all signals they can detect, chemical and mechanical ones alike, resulting in a response that is the consequence of all available information. As one signal may modulate the response of a cell to another signal48, perturbing mechanotransduction will likely alter the way in which neurons respond to chemical signals in the environment and vice versa. Furthermore, other cells in the vicinity of the OT that, for example, secrete signaling molecules such as semaphorin 3A or slits, might also be mechanosensitive. Manipulating mechanotransduction in these cells could then change chemical signals that contribute to controlling RGC growth. This intimate cross-talk between chemical and mechanical signaling supports the view that mechanosensing is just as critical as biochemical signaling for axon growth in the developing brain.

Axon pathfinding is a highly complex process; several chemical guidance cues have been shown to be important for instructing axon growth2–6. We have identified local tissue stiffness as another critical signal in a developing organism, which, together with membrane-bound and diffusible chemical cues, controls cell growth and tissue organization. Similar mechanical cell–tissue interactions are likely to be important for the

development of the CNS in general46 and in other organ systems across species. Mechanosensing is also likely to be critical for regenerative processes in which cells have to migrate or regrow through damaged tissue with altered mechanical properties.

Methods

Methods, including statements of data availability and any associated accession codes and references, are available in the online version of the paper.

Note: Any Supplementary Information and Source Data files are available in the online version of the paper.

Acknowledgments

We thank D. Bray, A. Reichenbach, B. Simons and S. Wolff for discussions about neuronal mechanics, K. Chalut and W. Harris for feedback on the manuscript, A. Christ for an AFM data analysis code, P. Moshayedi for help with establishing PAA gels, F. Sachs (University at Buffalo, USA) for providing GsMTx4, H. Wong for extensive help in the lab and A. Winkel and R. Field (JPK) for technical help. This work was supported by the German National Academic Foundation (scholarship to D.E.K.), Wellcome Trust and Cambridge Trusts (scholarships to A.J.T.), Winston Churchill Foundation of the United States (scholarship to S.K.F.), Herchel Smith Foundation (Research Studentship to S.K.F.), CNPq 307333/2013-2 (L.d.F.C.), NAP-PRP-USP and FAPESP 11/50761-2 (L.d.F.C.), UK EPSRC BT grant (J.G.), Wellcome Trust WT085314 and the European Research Council 322817 grants (C.E.H.); an Alexander von Humboldt Foundation Feodor Lynen Fellowship (K.F.), UK BBSRC grant BB/M021394/1 (K.F.), the Human Frontier Science Program Young Investigator Grant RGY0074/2013 (K.F.), the UK Medical Research Council Career Development Award G1100312/1 (K.F.) and the Eunice Kennedy Shriver National Institute Of Child Health & Human Development of the National Institutes of Health under Award Number R21HD080585 (K.F.). The content is solely the responsibility of the authors and does not necessarily represent the official views of the National Institutes of Health.

AUTHOR CONTRIBUTIONS

K.F. conceived the project; J.G., C.E.H. and K.F. designed the research; D.E.K., A.J.T., S.K.F., A.D., G.K.S., E.K.P., H.S. and K.F. performed the experiments; D.E.K., A.J.T., S.K.F., G.K.S., E.K.P., H.S., M.V., L.d.F.C. and K.F. analyzed the data; all authors discussed the data; K.F. wrote the manuscript with contributions from all authors.

COMPETINGFINANCIALINTERESTS

The authors declare no competing financial interests.

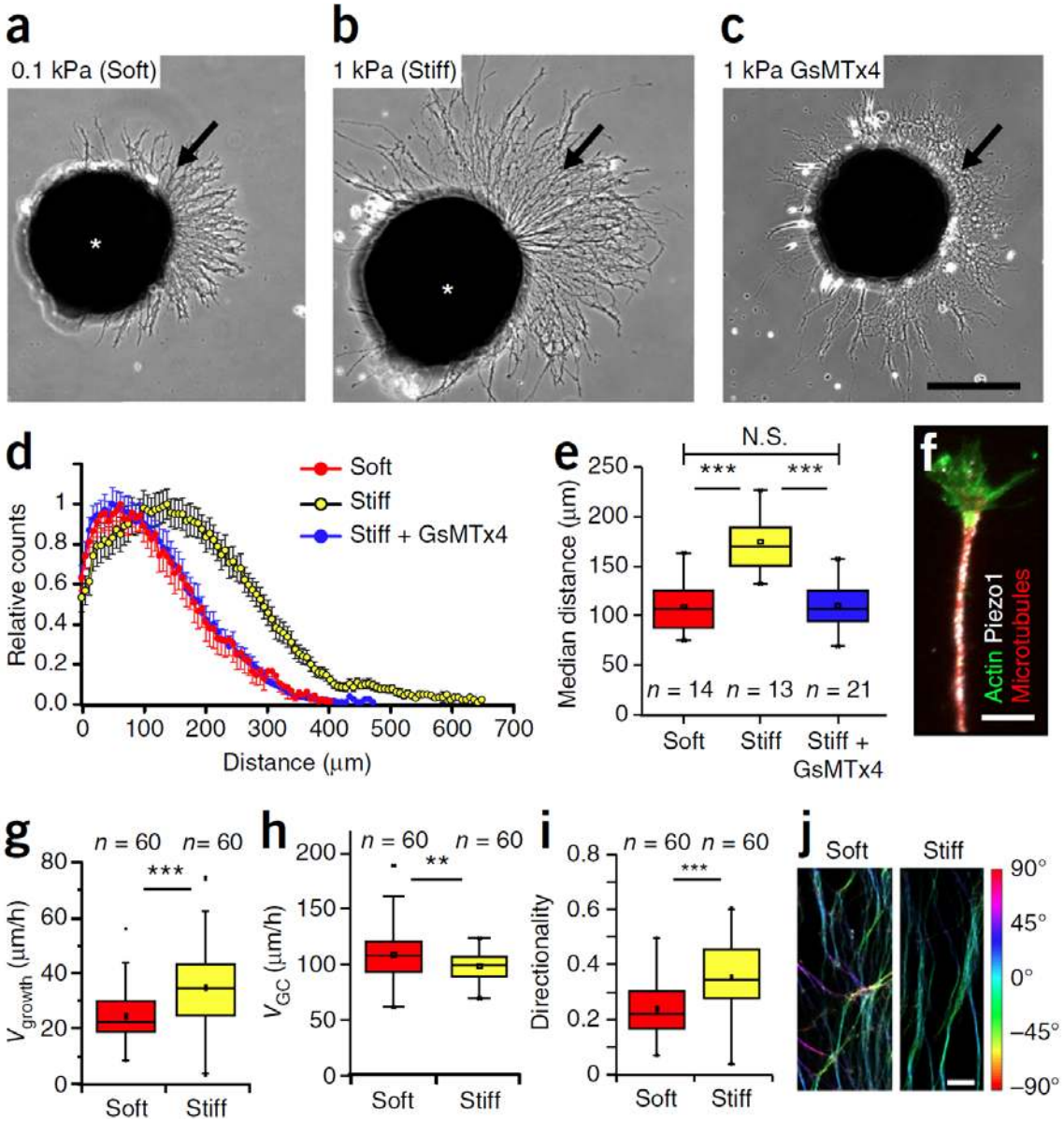

Figure 1 Mechanosensitivity of RGC axons *in vitro*. (**a**,**b**) Cultures of *Xenopus* eye primordia (asterisks) on (**a**) soft (0.1 kPa) and (**b**) stiff (1 kPa) substrates. Arrows indicate axons. (**c**) Eye primordium grown on a stiff substrate and treated with GsMTx4. Scale bar: 200 μm. (**d**) Sholl analysis of axon lengths after 24 h (normalized counts as mean ± s.e.m.). (**e**) Median distances shown in **d**. Axons were significantly longer on stiffer substrates than either on soft ones (one-way ANOVA followed by Bonferroni *post hoc* test; $P = 2.79 \times 10{-}7$, $t = 6.354$) or after GsMTx4 treatment ($P = 5.01 \times 10{-}8$, $t = -6.855$). Neurons grown on stiff substrates and treated with GsMTx4 resembled neurons grown on soft substrates ($P = 1.00$, $t = 0.082$). n = number of eye primordia from three biological replicates. (**f**) Immunocytochemistry showing f-actin (green), β-tubulin (red) and piezo1 (white). Scale bar: 10 μm. (**g**) The extension velocity of axons ($v$growth) was higher on stiff substrates (Mann-Whitney test; $P = 9.32 \times 10{-}6$, $z = 4.432$). (**h**) On soft substrates, growth cones (GC) explored their environment more and migrated significantly faster than on stiff ones (two-tailed t-test; $P = 0.00867$, $t = 2.669$). (**i**) On stiff substrates, axon growth was more directed (i.e., straighter) than on soft substrates (Mann-Whitney test; $P = 1.10 \times 10{-}6$, $z = 4.873$). n = number of axons from three biological replicates. (**j**) Processed fluorescence images of β-tubulin-labeled RGC axons; color represents local angular orientation of axonal segments. On soft substrates, axons grew less directionally persistently (from bottom to top; **Supplementary Fig. 2e–g**). Scale bar: 15 μm. All experiments were repeated 3 times, and representative images are shown. Boxes show the 25th, 50th (median), and 75th percentiles; whiskers show the spread of the data (excluding outliers), and an 'O' the mean score for a group. $^{**}P = 0.00867$; $^{***}P <$ 10−5; N.S., nonsignificant.

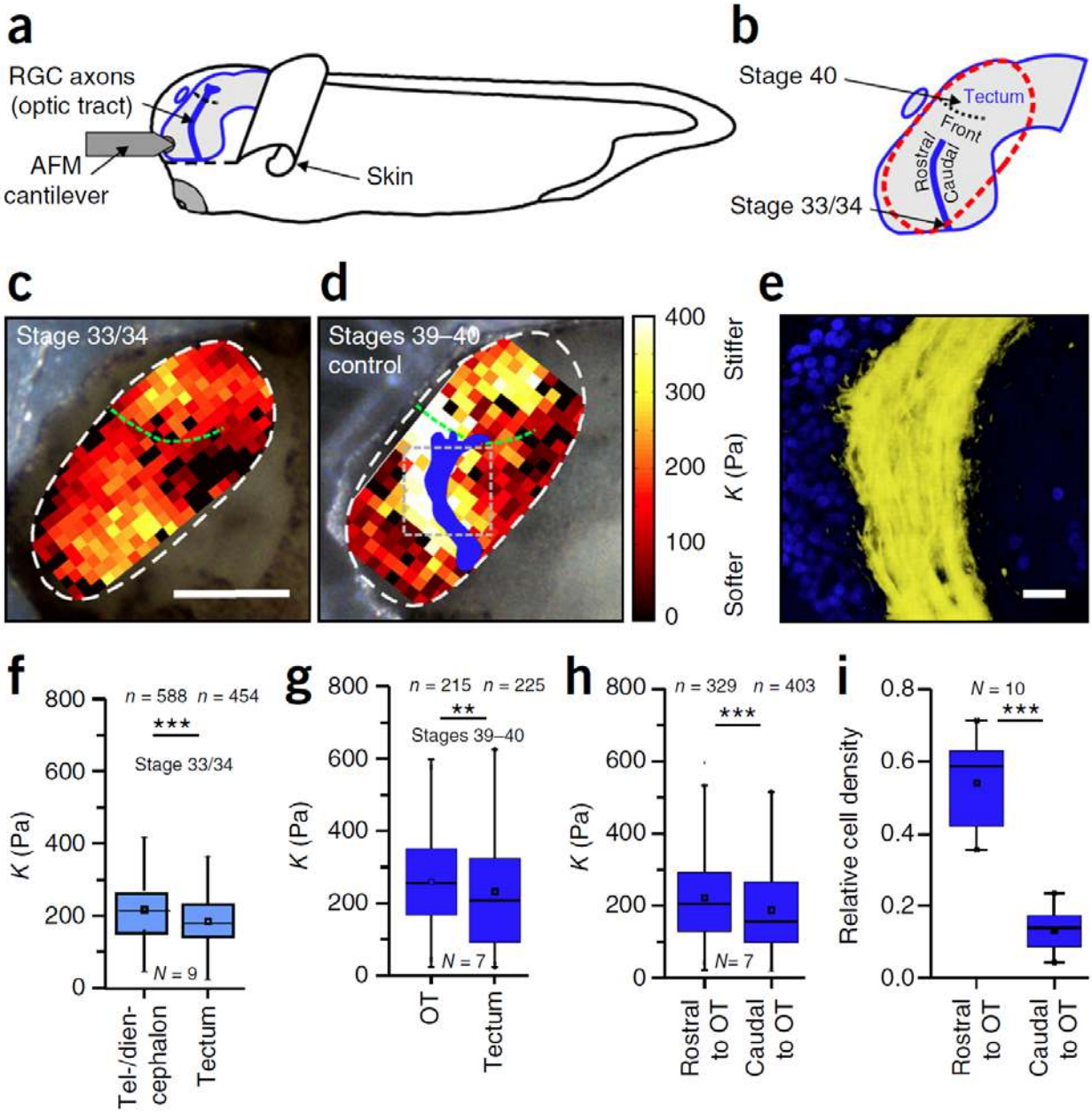

Figure 2 *In vivo* brain mechanics. (**a**) Schematic of the experimental setup. (**b**) *Xenopus* brain. The dashed red line indicates the stiffness map area. (**c**,**d**) Images of *Xenopus* embryos with overlaid AFM-based stiffness maps of exposed *in vivo* brain tissue. Color encodes the apparent elastic modulus *K* assessed at an indentation force of 7 nN. Blue shape in **d** shows the OT location (based on fluorescence images, **Supplementary Fig. 3**). Scale bar: 200 µm. At both stage 33/34 (**c**) and stages 39 and 40 (**d**), brain tissue was mechanically heterogeneous and displayed clearly visible stiffness gradients. Green dashed lines indicate tectum boundaries. The gray dashed square in **d** indicates a region as shown in **e**. (**e**) Immunohistochemistry demonstrated a significantly higher density of cell nuclei (blue) rostral to the OT (yellow) than caudal to it. Scale bar: 20 µm. (**f**) The tectum was softer than the telencephalon and diencephalon (tel-/diencephalon) at stage 33/34 (Mann-Whitney test; $P = 2.26 \times 10{-}9$, $z = 5.978$) and (**g**) than the OT at stages 39 and 40 ($P = 0.0033$, $z = 2.933$). (**h**) At stages 39 and 40, tissue rostral to the OT was significantly stiffer than caudal to it ($P = 2.97 \times 10{-}5$, $z = 4.163$). (**i**) Quantification of cell densities on both sides of the OT; cell density was significantly higher rostral to the OT (paired two-tailed *t*-test; $P = 3.96 \times 10{-}6$, $t = 9.879$). *n* = number of measurements, *N* = number of animals. All representative images and stiffness maps shown are from three biological replicates. Boxes show the 25th, 50th (median), and 75th percentiles; whiskers show the spread of the data (excluding outliers), and an 'O' the mean score for a group. $^{**}P = 0.0033$; $^{***}P < 10{-}4$.

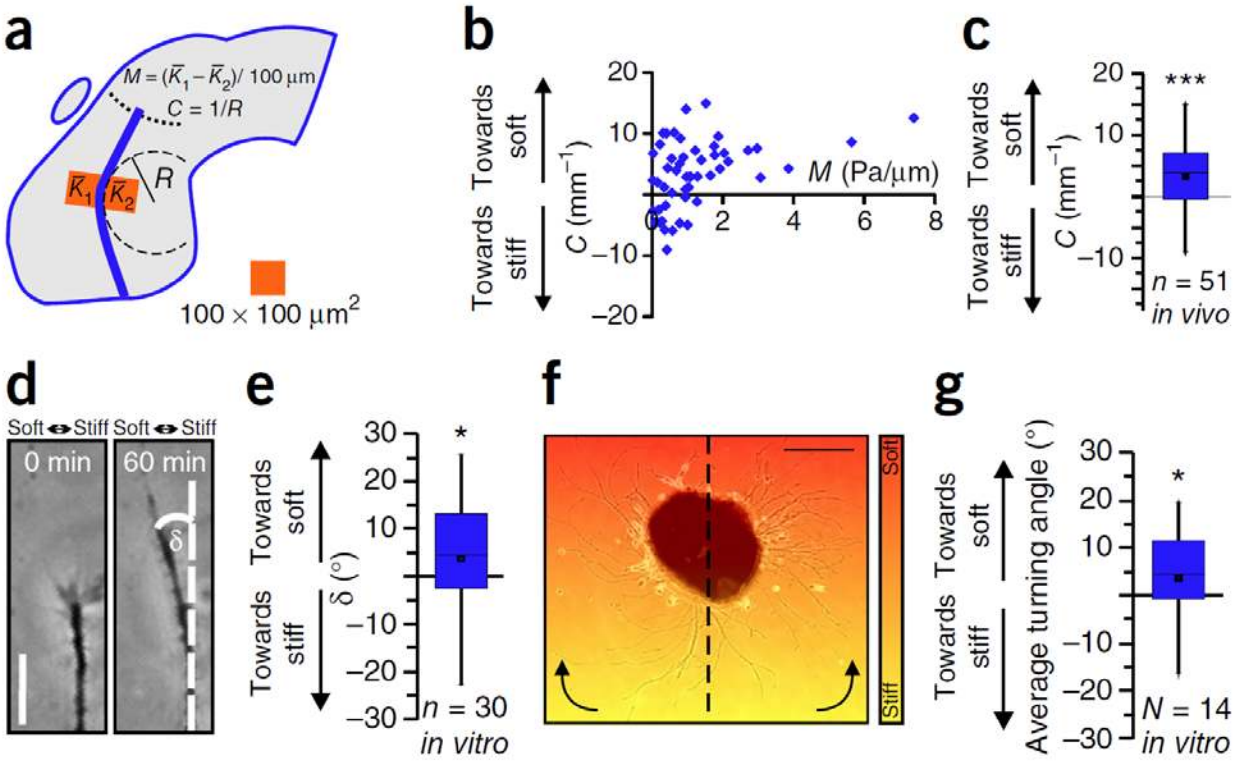

Figure 3 Neurons grow toward soft tissue. (**a**) Schematic showing how local gradients in brain tissue stiffness perpendicular to the RGC axon growth direction *M* and the local OT curvature *C* were determined. (**b**) Relationship between *M* and *C*. (**c**) Same data as in **b**, pooled. Axons *in vivo* preferentially turned toward the softer side of the tissue (one-sample Wilcoxon signed-rank test; $P = 1.44 \times 10{-}4$, $z = 3.801$). *n* = number of measurement points from 7 animals. (**d**,**e**) Time-lapse imaging of individual axon bundles growing on a stiffness gradient matching that found *in vivo* (*M*max = ~2 Pa/µm; **Supplementary Fig. 1**) revealed that *in vitro*, in the absence of chemical gradients, RGC axons preferentially turned toward the softer side of the substrate (one-sample Wilcoxon signed-rank test; $P = 0.0549$; $z = -1.913$). Scale bar: 20 µm. Representative images from 11 biological replicates are shown. (**f**) Eye primordium cultured on a similar stiffness gradient (indicated by color). Axons growing more clockwise in the left half and more counterclockwise in the right half of the image turned toward the soft side of the substrate. Scale bar: 200 µm. The experiment was repeated three times, and a representative image is shown. (**g**) Quantification of individual axon segment orientations similarly revealed preferential turning toward the soft side of the substrate (one-sample Wilcoxon signed-rank test; $P = 0.0264$, $z = 2.197$). Boxes show the 25th, 50th (median), and 75th percentiles; whiskers show the spread of the data (excluding outliers), and an 'O' the mean score for a group. $^{*}P \leq 0.05$; $^{***}P = 1.44 \times 10{-}4$.

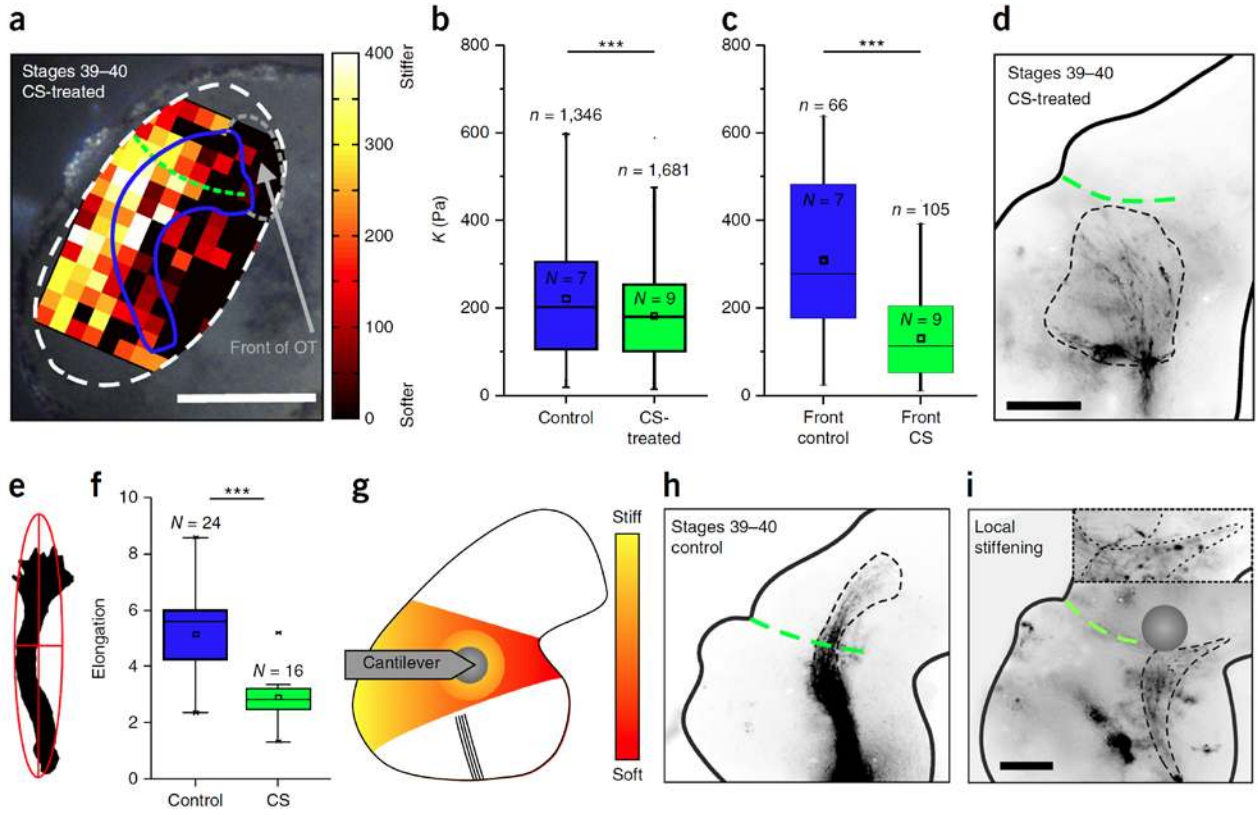

Figure 4 Perturbing brain stiffness leads to axonal pathfinding errors. (**a**) *Xenopus* brain treated with 15 mg/ml CS, overlaid with an AFM-based stiffness map. Blue curve, OT location (based on fluorescence images; **Supplementary Fig. 3**); green dashed curve, tectum boundary; gray dashed line, region in front of the OT. Scale bar: 200 µm. (**b**) Tissue was significantly stiffer in control brains (blue) compared to CS-treated brains (green) (Mann-Whitney test; $P = 6.62 \times 10{-}10$, $z = 6.175$), particularly in front of the OT (**c**) ($P = 8.57 \times 10{-}11$, $z = 6.490$). n = number of measurements, N = number of animals. (**d**) Image of CS-treated, softened brain. The dashed black curve indicates the outline of the OT. RGC axons dispersed widely from their normal trajectory. Scale bar: 100 µm. (**e**) Example of a fit of an ellipse around the outline of an OT; the ratio of long and short axes determines the elongation. (**f**) CS treatment significantly decreased the elongation of the OT (two-tailed t-test; $P = 3.12 \times 10{-}6$, $t = 5.462$). N = number of animals. (**g**) Schematic illustration of local mechanical brain manipulation. Soft tissue caudal to the presumptive caudal turn of the OT was locally indented with an AFM cantilever for ~6 h. (**h**) In control brains, the OT grew normally. (**i**) When a force was locally exerted on the tissue (position of the probe is indicated by the filled gray circle), axons grew away from the cantilever probe, thus deviating from their normal pathway. Inset: magnification of the distal part of the OT. Scale bar: 100 µm. All experiments were repeated three times, and representative images are shown. Boxes show the 25th, 50th (median), and 75th percentiles; whiskers show the spread of the data (excluding outliers), and an 'O' the mean score for a group. ***$P < 10{-}5$.

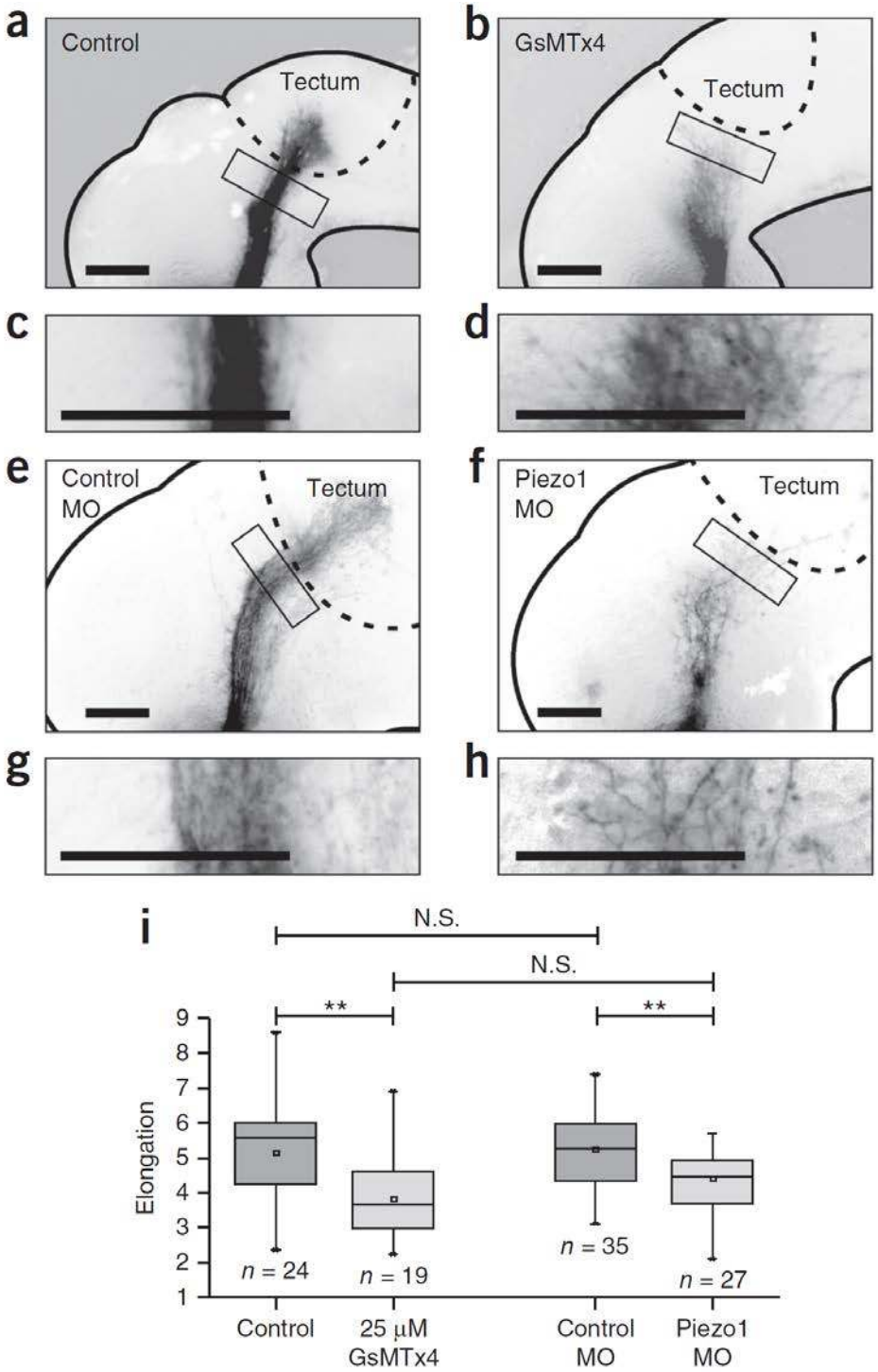

Figure 5 *In vivo* manipulation of mechanosensitive ion channels disrupts axon pathfinding. (**a**–**d**) The application of 25 µM GsMTx4 disrupted axon pathfinding *in vivo*. Axons were shorter and spread more, resembling axons cultured on soft substrates *in vitro*. (**c**,**d**) Enlargements of boxes shown in **a** and **b**, respectively. (**e**–**h**) Similarly, morpholino (MO) knockdown of piezo1 led to aberrant axon growth *in vivo*. Scale bars: 100 µm. Experiments were repeated three (**a**–**d**) or four times (**e**–**h**), and representative images are shown. (**i**) Quantification of OT morphology. Interfering with mechanotransduction led to a significantly decreased elongation of the OT (two-tailed *t*-test; *P*GsMTx4 = 0.00243, *t* = 3.231; *P*piezo1–MO = 0.00476, *t* = 2.932). Phenotypes of controls were similar (*P* = 0.782, *t* = 0.278), as well as those of GsMTx4-treated and piezo1 knockdown animals (*P* = 0.0976, *t* = 1.692). *n* = number of animals. Boxes show the 25th, 50th (median), and 75th percentiles; whiskers show the spread of the data (excluding outliers), and an 'O' the mean score for a group. $^{**}P < 0.01$; N.S., nonsignificant.

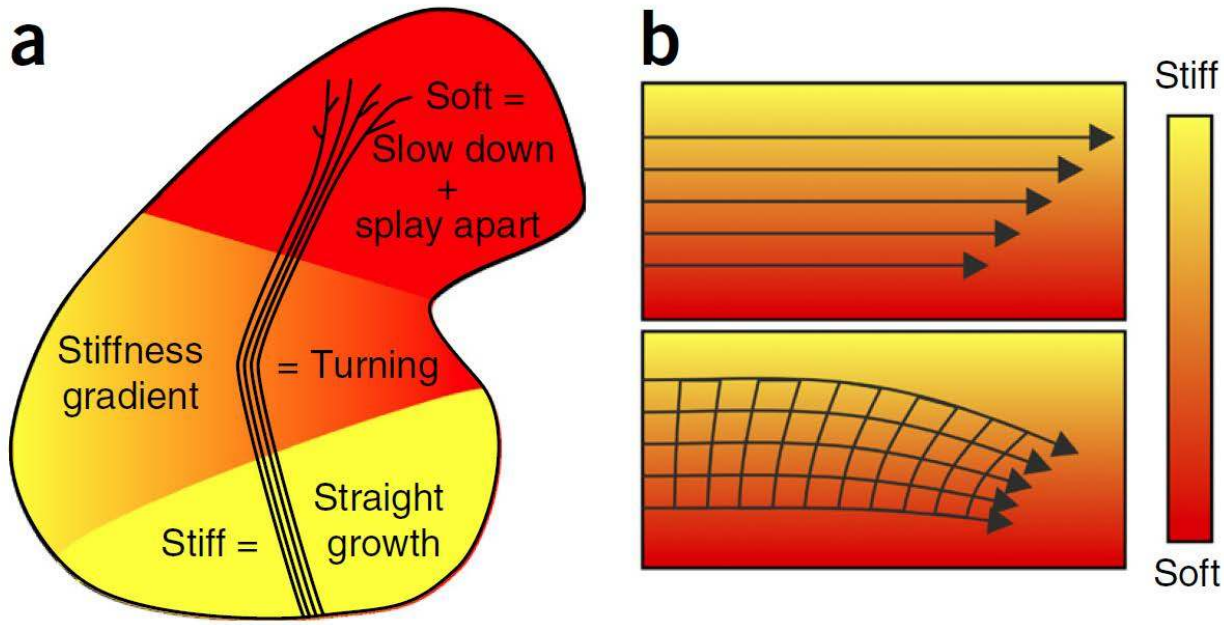

Figure 6 Schematics of the mechanical control of axon growth. (**a**) Schematic summary of this study. Shown is the outline of a *Xenopus* brain and the OT. Mechanical signals contribute to neuronal growth in the developing CNS. RGC axons grow faster, straighter, and more parallel on stiffer than on softer substrates (**Fig. 1**). Accordingly, the part of the brain these axons have to pass is stiffer than the tectum (**Fig. 2**), where axon growth slows down and eventually stops. The softness of the tectum then facilitates unbundling and branching. On their way, axons encounter an area with a stiffness gradient, which contributes to the turning of the OT toward the softer side of the brain (**Fig. 3**). (**b**) Schematic illustration of a mechanism by which axon bundles encountering a perpendicular stiffness gradient might turn toward the softer side of the substrate. The velocity of axons is larger on stiffer substrates (upper panel). As axons in the OT fasciculate, they are mechanically coupled, so the faster axons growing on the stiffer side may be pulled toward the slower axons on the softer side, leading to a reorientation of the axon bundle and overall growth toward the softer side.

1. Sperry, R.W. Chemoaffinity in the orderly growth of nerve fiber patterns and connections. *Proc. Natl. Acad. Sci. USA* **50**, 703–710 (1963).

2. Tessier-Lavigne, M. & Goodman, C.S. The molecular biology of axon guidance. *Science* **274**, 1123–1133 (1996).

3. Erskine, L. & Herrera, E. The retinal ganglion cell axon's journey: insights into molecular mechanisms of axon guidance. *Dev. Biol.* **308**, 1–14 (2007).

4. Campbell, D.S. *et al.* Semaphorin 3A elicits stage-dependent collapse, turning, and branching in *Xenopus* retinal growth cones. *J. Neurosci.* **21**, 8538–8547 (2001).

5. Piper, M. *et al.* Signaling mechanisms underlying Slit2-induced collapse of *Xenopus* retinal growth cones. *Neuron* **49**, 215–228 (2006).

6. Atkinson-Leadbeater, K. *et al.* Dynamic expression of axon guidance cues required for optic tract development is controlled by fibroblast growth factor signaling. *J. Neurosci.* **30**, 685–693 (2010).

7. Chan, C.E. & Odde, D.J. Traction dynamics of filopodia on compliant substrates. *Science* **322**, 1687–1691 (2008).

8. Moore, S.W., Biais, N. & Sheetz, M.P. Traction on immobilized netrin-1 is sufficient to reorient axons. *Science* **325**, 166 (2009).

9. Betz, T., Koch, D., Lu, Y.B., Franze, K. & Käs, J.A. Growth cones as soft and weak force generators. *Proc. Natl. Acad. Sci. USA* **108**, 13420–13425 (2011).

10. Koch, D., Rosoff, W.J., Jiang, J., Geller, H.M. & Urbach, J.S. Strength in the periphery: growth cone biomechanics and substrate rigidity response in peripheral and central nervous system neurons. *Biophys. J.* **102**, 452–460 (2012).

11. Weiss, P. In vitro experiments on the factors determining the course of the outgrowing nerve fiber. *J. Exp. Zool.* **68**, 393–448 (1934).

12. Flanagan, L.A., Ju, Y.E., Marg, B., Osterfield, M. & Janmey, P.A. Neurite branching on deformable substrates. *Neuroreport* **13**, 2411–2415 (2002).

13. Georges, P.C., Miller, W.J., Meaney, D.F., Sawyer, E.S. & Janmey, P.A. Matrices with compliance comparable to that of brain tissue select neuronal over glial growth in mixed cortical cultures. *Biophys. J.* **90**, 3012–3018 (2006).

14. Kostic, A., Sap, J. & Sheetz, M.P. RPTPalpha is required for rigidity-dependent inhibition of extension and differentiation of hippocampal neurons. *J. Cell Sci.* **120**, 3895–3904 (2007).

15. Jiang, F.X., Yurke, B., Schloss, R.S., Firestein, B.L. & Langrana, N.A. Effect of dynamic stiffness of the substrates on neurite outgrowth by using a DNA-crosslinked hydrogel. *Tissue Eng. Part A* **16**, 1873–1889 (2010).

16. Balgude, A.P., Yu, X., Szymanski, A. & Bellamkonda, R.V. Agarose gel stiffness determines rate of DRG neurite extension in 3D cultures. *Biomaterials* **22**, 1077–1084 (2001).

17. Elkin, B.S., Azeloglu, E.U., Costa, K.D. & Morrison, B. III. Mechanical heterogeneity of the rat hippocampus measured by atomic force microscope indentation. *J. Neurotrauma* **24**, 812–822 (2007).

18. Christ, A.F. *et al.* Mechanical difference between white and gray matter in the rat cerebellum measured by scanning force microscopy. *J. Biomech.* **43**, 2986–2992 (2010).

19. Franze, K. *et al.* Spatial mapping of the mechanical properties of the living retina using scanning force microscopy. *Soft Matter* **7**, 3147–3154 (2011).

20. Iwashita, M., Kataoka, N., Toida, K. & Kosodo, Y. Systematic profiling of spatiotemporal tissue and cellular stiffness in the developing brain. *Development* **141**, 3793–3798 (2014).

21. Elkin, B.S., Ilankovan, A. & Morrison, B. III. Age-dependent regional mechanical properties of the rat hippocampus and cortex. *J. Biomech. Eng.* **132**, 011010 (2010).

22. Koser, D.E., Moeendarbary, E., Hanne, J., Kuerten, S. & Franze, K. CNS cell distribution and axon orientation determine local spinal cord mechanical properties. *Biophys. J.* **108**, 2137–2147 (2015).

23. Weickenmeier, J. *et al.* Brain stiffness increases with myelin content. *Acta Biomater.* **42**, 265–272 (2016).

24. Moshayedi, P. *et al.* Mechanosensitivity of astrocytes on optimized polyacrylamide gels analyzed by quantitative morphometry. *J. Phys. Condens. Matter* **22**, 194114 (2010).

25. Franze, K., Janmey, P.A. & Guck, J. Mechanics in neuronal development and repair. *Annu. Rev. Biomed. Eng.* **15**, 227–251 (2013).

26. Guan, W., Puthenveedu, M.A. & Condic, M.L. Sensory neuron subtypes have unique substratum preference and receptor expression before target innervation. *J. Neurosci.* **23**, 1781–1791 (2003).

27. Franze, K. *et al.* Neurite branch retraction is caused by a threshold-dependent mechanical impact. *Biophys. J.* **97**, 1883–1890 (2009).

28. Kerstein, P.C. *et al.* Mechanosensitive TRPC1 channels promote calpain proteolysis of talin to regulate spinal axon outgrowth. *J. Neurosci.* **33**, 273–285 (2013).

29. Zhang, Q.Y. *et al.* Stiff substrates enhance cultured neuronal network activity. *Sci. Rep.* **4**, 6215 (2014).

30. Shibasaki, K., Murayama, N., Ono, K., Ishizaki, Y. & Tominaga, M. TRPV2 enhances axon outgrowth through its activation by membrane stretch in developing sensory and motor neurons. *J. Neurosci.* **30**, 4601–4612 (2010).

31. Pathak, M.M. *et al.* Stretch-activated ion channel Piezo1 directs lineage choice in human neural stem cells. *Proc. Natl. Acad. Sci. USA* **111**, 16148–16153 (2014).

32. Coste, B. *et al.* Piezo1 and Piezo2 are essential components of distinct mechanically activated cation channels. *Science* **330**, 55–60 (2010).

33. Coste, B. *et al.* Piezo proteins are pore-forming subunits of mechanically activated channels. *Nature* **483**, 176–181 (2012).

34. Kim, S.E., Coste, B., Chadha, A., Cook, B. & Patapoutian, A. The role of *Drosophila* Piezo in mechanical nociception. *Nature* **483**, 209–212 (2012).

35. Li, J. *et al.* Piezo1 integration of vascular architecture with physiological force. *Nature* **515**, 279–282 (2014).

36. Gottlieb, P.A. & Sachs, F. Piezo1: properties of a cation selective mechanical channel. *Channels (Austin)* **6**, 214–219 (2012).

37. Kanekar, S. *et al.* Xath5 participates in a network of bHLH genes in the developing Xenopus retina. *Neuron.* **19**, 981–994 (1997).

38. Swift, J. *et al.* Nuclear lamin-A scales with tissue stiffness and enhances matrix-directed differentiation. *Science* **341**, 1240104 (2013).

39. Majkut, S. *et al.* Heart-specific stiffening in early embryos parallels matrix and myosin expression to optimize beating. *Curr. Biol.* **23**, 2434–2439 (2013).

40. Walz, A., Anderson, R.B., Irie, A., Chien, C.B. & Holt, C.E. Chondroitin sulfate disrupts axon pathfinding in the optic tract and alters growth cone dynamics. *J. Neurobiol.* **53**, 330–342 (2002).

41. Pogoda, K. *et al.* Compression stiffening of brain and its effect on mechanosensing by glioma cells. *New J. Phys.* **16**, 075002 (2014).

42. Lo, C.M., Wang, H.B., Dembo, M. & Wang, Y.L. Cell movement is guided by the rigidity of the substrate. *Biophys. J.* **79**, 144–152 (2000).

43. Isenberg, B.C., Dimilla, P.A., Walker, M., Kim, S. & Wong, J.Y. Vascular smooth muscle cell durotaxis depends on substrate stiffness gradient strength. *Biophys. J.* **97**, 1313–1322 (2009).

44. Bollmann *et al.* Microglia mechanics: immune activation alters traction forces and durotaxis. *Front. Cell Neurosci.* **9**, 363 (2015).

45. Xu, G. *et al.* Opening angles and material properties of the early embryonic chick brain. *J. Biomech. Eng.* **132**, 011005 (2010).

46. Franze, K. The mechanical control of nervous system development. *Development* **140**, 3069–3077 (2013).

47. Singh, T., Meena, R. & Kumar, A. Effect of sodium sulfate on the gelling behavior of agarose and water structure inside gel networks. *J. Phys. Chem. B* **113**, 2519–2525 (2009).

48. Höpker, V.H., Shewan, D., Tessier-Lavigne, M., Poo, M. & Holt, C. Growth-cone attraction to netrin-1 is converted to repulsion by laminin-1. *Nature* **401**, 69–73 (1999).

49. Nieuwkoop, P.D. & Faber, J. *Normal table of* Xenopus laevis *(Daudin): a Systematical and Chronological Survey of the Development from the Fertilized Egg till the End of Metamorphosis* (North-Holland Pub. Co., 1967).

50. Das, T., Payer, B., Cayouette, M. & Harris, W.A. *In vivo* time-lapse imaging of cell divisions during neurogenesis in the developing zebrafish retina. *Neuron* **37**, 597–609 (2003).

51. Chien, C.B., Rosenthal, D.E., Harris, W.A. & Holt, C.E. Navigational errors made by growth cones without filopodia in the embryonic *Xenopus* brain. *Neuron* **11**, 237–251 (1993).

52. Leung, K.M. *et al.* Asymmetrical beta-actin mRNA translation in growth cones mediates attractive turning to netrin-1. *Nat. Neurosci.* **9**, 1247–1256 (2009).

53. Kalous, A., Stake, J.I., Yisraeli, J.K. & Holt, C.E. RNA-binding protein Vg1RBP regulates terminal arbor formation but not long-range axon navigation in the developing visual system. *Dev. Neurobiol.* **74**, 303–318 (2014).

54. Wizenmann, A. *et al.* Extracellular Engrailed participates in the topographic guidance of retinal axons in vivo. *Neuron* **64**, 355–366 (2009).

55. Hutter, J.L. & Bechhoefer, J. Calibration of atomic-force microscope tips. *Rev. Sci. Instrum.* **64**, 1868–1873 (1993).

56. Mahaffy, R.E., Shih, C.K., MacKintosh, F.C. & Käs, J. Scanning probe-based frequency-dependent microrheology of polymer gels and biological cells. *Phys. Rev. Lett.* **85**, 880–883 (2000).

57. Franze, K. Atomic force microscopy and its contribution to understanding the development of the nervous system. *Curr. Opin. Genet. Dev.* **21**, 530–537 (2011).

58. Sholl, D.A. Dendritic organization in the neurons of the visual and motor cortices of the cat. *J. Anat.* **87**, 387–406 (1953).

59. Hertz, H. Über die Berührung fester elastischer Körper. *J. Reine Angew. Math.* **92**, 156–171 (1881).

60. Tamada, A., Kawase, S., Murakami, F. & Kamiguchi, H. Autonomous right-screw rotation of growth cone filopodia drives neurite turning. *J. Cell Biol.* **188**, 429–441 (2010).

ONLINE METHODS

All chemicals were obtained from Sigma-Aldrich and all antibodies were obtained from Abcam if not otherwise noted.

Preparation of polyacrylamide hydrogels. *Plain substrates.* Compliant polyacrylamide (PAA) hydrogel culture substrates were prepared as described previously24. Briefly, 21-mm glass-bottom Petri dishes (μ-Dish35mm, high; Ibidi, Germany) were dabbed with a 0.1 N NaOH solution using a cotton bud and air-dried. The glass was then treated with 200 μl (3-aminopropyl)trimethoxysilane (APTMS) for 3 min and washed with distilled water. 400 μl of 0.5% glutaraldehyde solution was then added for 30 min. Petri dishes were again washed and air-dried. Glass coverslips 19 mm in diameter were cleaned with 70% ethanol and distilled water and then treated with Rain-X solution (Shell Car Care International Ltd, UK) for 10 min, resulting in a nonadhesive coating. Rain-X solution was removed and the coverslips dried using lint-free wipes.

The shear storage modulus G' of the PAA gel was adjusted using predefined ratios of 60% phosphate buffered saline (PBS; Fisher Scientific, UK), 40% (w/v) acrylamide (AA) solution and 2% bis-acrylamide (Bis-AA) solution (Fisher Scientific, UK), as described previously24. Gel premix solutions (500 μl) corresponding to ~0.1 kPa (5% AA & 0.04% Bis-AA) and 1 kPa (7.5% AA and 0.06% Bis-AA) were desiccated for 10 min. Polymerization was initiated by addition of 5 μL freshly prepared 10% ammonium persulfate (APS) and 1.5 μL N,N,N′,N′-tetramethylethylenediamine (TEMED) to the PAA premixes. Forty microliters (40 μL) of this solution was pipetted onto the treated glass-bottom Petri dish and then covered with the Rain-X-coated coverslip. After 15 min, coverslips were submerged in PBS for a further 20 min before the top coverslip was removed. Gels were then washed in filter-sterilized 60% PBS three times and functionalized with 5–10 μg/ml laminin (from Engelbreth-Holm-Swarm murine sarcoma basement membrane) for 2 h before culturing, or 1 μg/ml fibronectin (from bovine plasma) for 3 h before culturing. To allow laminin or fibronectin to adhere to the substrates, gels were prepared either by incubating them in hydrazine hydrate for 4 h, 5% acetic acid solution (Fisher Scientific, UK) for 1 h, sterile 60% PBS (washed 3 times), 10 or 100 μg/ml poly-d-lysine solution (PDL; MW 70,000–150,000) overnight at 4 °C and sterile 60% Leibovitz L15 medium, washed three times24, or by incubating them in 40 μg/ml Cell-Tak™ (BD Biosciences, UK) for 2 h at room temperature and subsequently washing them in sterile 60% PBS10.

Gradient substrates. Substrates incorporating stiffness gradients with a similar strength to those we found *in vivo* were produced by filling custom-designed chambers first with PAA gel premixes for ~10 kPa (12% AA & 0.2% Bis-AA) immediately after polymerization was initiated, and then with 0.1 kPa gel premixes (see above). In the 10 kPa premix, 5 μl PBS were substituted by 5 μl of 1% (w/v) fluorescein O,O′-dimethacrylate diluted in DMSO. Diffusion led to a linear gradient in stiffness and fluorescence signal (**Supplementary Fig. 1**).

Gel chambers were assembled from two Parafilm-covered microscope slides, enclosing a glutaraldehyde-treated coverslip 22 × 22 mm2 and a RainX-treated coverslip 22 × 40 mm2, which were placed with the treated sides facing each other but separated by a U-shaped Parafilm spacer. Chambers were held together with bulldog clips and stood vertically, with the gap between the two coverslips at the top, into which the gel premixes were pipetted (**Supplementary Fig. 1**).

Substrate coating measurements. PAA gels were coated with 10 μg/ml laminin as described above. Substrates were then incubated overnight (18 h) at room temperature with 300 μL of a polyclonal rabbit anti-laminin antibody (ab11575) diluted at 1:200 with PBS and 1% bovine serum albumin (BSA). Gels were then washed (four times for 10 min each time) with PBS and subsequently incubated for 4 h in secondary antibody solution (donkey anti-rabbit Alexa Fluor® 488; Invitrogen, A-21206, 1:1,000 dilution) containing 1% BSA in PBS. Gels were washed again (five times for 10 min each time) with PBS and imaged immediately using a Nikon Eclipse Ni-E microscope (60× W; NA = 1.0). Twenty-four images were captured from each gel (3 gels per group). For each image, 6 distinct regions of interest were randomly chosen and the mean fluorescence intensity calculated using ImageJ software (NIH, MD, USA).

Animal model. All animal experiments were approved by the Ethical Review Committee of the University of Cambridge and complied with Home Office guidelines. *Xenopus laevis* embryos of both sexes were obtained by *in vitro* fertilization, raised in 0.1× Modified Barth's Saline (MBS) at 14–18 °C, and staged according to the tables of Nieuwkoop and Faber49. For AFM experiments, embryos were injected in one blastomere at the 4-cell stage with an Ath5:mGFP construct50 (50 pg/5 nl) in order to label RGC axons in one retina. Fluorescently labeled RGC axons crossed the optic chiasm into the unlabeled brain, allowing visualization of the OT for AFM experiments.

For ablated eye primordia experiments, in which brains not containing RGC axons were measured by AFM at stages 39 and 40, stage 31 and 32 embryos were transferred to MR solution51 (composition: 1× MBS with 0.04% (w/v) MS222 anesthetic (3-aminobenzoic acid ethyl ester methanesulfonate) and 1× penicillin/streptomycin/Fungizone (P/S/F; Life Technologies, UK), pH 7.4) and both eye primordia carefully removed with 0.1 mm minutien pins. Embryos were allowed to recover at 18 °C in 0.5× MBS + 0.02% (w/v) MS222 for 1 h, followed by 0.25× MBS + 0.01% (w/v) MS222 overnight. Embryos were then transferred to 0.1× MBS and left at 18 °C to reach stages 39 and 40.

For *ex vivo* eye primordia cell culture experiments, stage 33/34 or 35/36 embryos were transferred to a 35-mm Petri dish coated with Sylgard® 184 and anesthetized with 0.04% (w/v) MS222 solution (24.75 ml 10× MBS, 250 μl 100× P/S/F, and 100 mg MS222 dissolved in 225 ml ddH2O, adjusted to pH 7.7 and filter-sterilized). Whole eye primordia were dissected, placed onto PAA hydrogels and cultured at 20 °C for 24–36 h in culture medium. *Xenopus* culture medium was composed of 60% L15 medium, 100 U/ml penicillin, 100 μg/ml streptomycin and 2.5 μg/mL amphotericin B (Life Technologies, UK), pH 7.7.

For GsMTx4 treatment experiments, 1–5 μM GsMTx4 (from F. Sachs (University at Buffalo, USA) and Abcam, ab141871) was added to eye primordia 2 h after they had been placed on gels. After an additional 22 h of incubation, explants were fixed in 2% PFA + 7.5% sucrose for 25 min and washed several times with 100% PBS before imaging.

Exposed brain preparations. Exposed brain experiments were carried out in MR solution51. Stage 33/34 embryos were transferred to a 35-mm Petri dish coated with Sylgard® 184 and immobilized with bent 0.2 mm minutien pins with the side of the body facing up. Skin, dura and eye were carefully dissected out using fine forceps and a 0.1 mm minutien pin to expose the brain from the dorsal to ventral midline and from the hindbrain, just anterior of the otic (auditory) vesicle, to the telencephalon. The embryos were then transferred to a 4-well plate and submerged in solution containing either MR alone (control), or MR + 25 μM

GsMTx4 or MR + 15 mg/ml chondroitin sulfate, and kept in the incubator at 14 or 18 °C until reaching stages 39 and 40.

Morpholino injections. Fluorescein-tagged translation-blocking morpholino oligonucleotides (MOs) against *piezo1* (5′-CACAGAGGACTTGCAGTTCCATCCC-3′) were designed and synthetized by GeneTools (GeneTools, OR, USA). We injected 15 ng of piezo1 MO or control scrambled MO (GeneTools, OR, USA; 5′-CCTCTTACCTCAGTTACAATTTATA-3′) into each dorsal blastomere of 4-cell-stage embryos, as described previously52. The embryos were transferred to a 14 °C incubator until stage 40, when they were imaged.

Western blots. Heads of stage 39–41 *Xenopus* embryos were dissected from control animals, control (scrambled) MO-injected animals and those injected with piezo1 MO as described above. While for the characterization of axon growth only the healthiest embryos (which looked closest in phenotype to the controls) were taken, for western blot analysis all embryos containing the morpholino were used. Heads were homogenized in a protease inhibitor cocktail diluted in lysis buffer (NaCl 150 mM, Triton X-100 1%, sodium deoxycholate 0.5%, sodium dodecyl sulfate 4 mg/ml, Tris buffer 50 mM; pH 8), with 1× Halt Protease and Phosphatase Inhibitor Cocktail (Thermo Scientific, UK), and protein samples were prepared for western blot as described previously53. The Bradford calorimetric assay (Bio-Rad Protein Assay Dye Reagent Concentrate, #5000006; Bio-Rad Laboratories, UK) was used to calculate total protein concentration and the loading volume adjusted accordingly. Samples were run on 4–15% SDS-PAGE gradient gels (Bio-Rad Laboratories, UK) and transferred to a nitrocellulose membrane. Membranes were blocked for 1 h in a blocking solution of 5% skim milk powder diluted in TBS-T (pH 7.4), and incubated overnight at 4 °C with a polyclonal rabbit anti-piezo1 (anti-FAM38A) primary antibody (ab82336; 1:500 dilution), and monoclonal mouse anti-α-tubulin (ab7291; 1:8,000 dilution) as a loading control. Excess primary antibodies were then washed off and the nitrocellulose membrane incubated for 1 h at room temperature (18–22 °C) in polyclonal goat anti-rabbit antibody conjugated to horseradish peroxidase (HRP) (ab97069; 1:2,000 dilution) for piezo1, and a polyclonal goat anti-mouse antibody conjugated to HRP (ab6789; 1:15,000 dilution) secondary for α-tubulin. Western blots were developed using Novex ECL HRP Chemiluminescent Substrate Reagent kit (Invitrogen, CA, USA) and an X-ray developer. Densitometry was performed on 8-bit greyscale images imported into Fiji software (NIH, MD, USA). The Gel analysis tool was used to correct for background and to measure relative band intensities. The ratio of relative intensities of piezo1 to α-tubulin was used to compare different groups.

Imaging of axons *in situ*. For morphological characterization, eye primordia were imaged after 24 h in culture by phase-contrast microscopy on a Nikon Eclipse TE2000-U or a Zeiss AxioObserver A1 microscope (10× Ph1, NA = 0.3). For time-lapse imaging of axon growth, eye primordia were imaged after 18–24 h in culture using a Nikon Eclipse TE3000 microscope (10× Ph1 objective, NA = 0.25). Images were captured every 30 s for ~3 h using a CCD camera (AxioCam ERc 5s, Zeiss, UK) and ZEN 2011 software. For turning assays (see below), axons were imaged after 12–24 h in culture using a Nikon Eclipse TE3000 (20× Ph1, NA = 0.45). Images were captured every 30 s using a Hamamatsu c4742-95 camera (Hamamatsu Photonics, Japan) and OpenLab software.

Immunofluorescence. To visualize axons for orientation analysis (see below), eye primordia were fixed after 24 h in 2% PFA + 7.5% sucrose and stained for β-tubulin (primary: ab6046, 1:1,000; secondary: ab175470,

1:1,000). Actin was visualized with phalloidin (A12379; Life Technologies, UK). Images were taken of axons close to eye primordia using a Zeiss AxioObserver.A1 (40× water immersion objective, NA = 1.1) and an sCMOS camera (Zyla 4.2, Andor). To study the piezo1 distribution, eye primordia were cultured on glass-bottom microwell dishes (MatTek, MA, USA) fixed as above, stained with β-tubulin (primary: ab6046, 1:1,000; secondary: ab150075, 1:1,000) and piezo1 (primary: Santa Cruz Biotechnology, sc-164319, 1:200; secondary: ab175704, 1:1,000); actin was visualized with phalloidin (A12379; Life Technologies, UK). Images of axons and growth cones were taken using a Nikon Eclipse TE2000-U inverted fluorescence microscope (60× oil immersion, NA = 1.4).

OTimaging in intact brains. To visualize the OT and cell nuclei for cell density measurements, the lens primordia of stage 40 embryos were removed and a plug of semidried HRP (30% HRP in 1% lysolecithin) was placed in the lens cavity. Embryos were fixed 30 min later in 4% paraformaldehyde for 1 h at room temperature. After fixation, brains were dissected and reacted with diaminobenzidine (DAB; 1 DAB tablet dissolved into 15 ml 0.1 M Tris buffer and 12 µl 30% H2O2). Nuclei were labeled using 4,6-diamidino-2-phenylindole (DAPI, 1 µg ml−1). Brains were mounted in Fluoromount-G (eBioscience, UK), and the lateral view of the OT was imaged using a confocal microscope (SP8, Leica Microsystems, UK; 20× objective, N.A. = 0.75).

To visualize the OT in mechanically manipulated brains, embryos were fixed in 4% paraformaldehyde overnight at 4 °C. DiI crystals were diluted in ethanol and injected at the boundary between lens and the retina as previously described54. After 24 h of incubation at room temperature, brains were dissected out and mounted in PBS, and the lateral view of the OT was imaged using a Nikon Eclipse 80i microscope (10×, NA = 0.3; and 20×, NA = 0.75).

***In vivo* AFM experiments.** Tipless silicon cantilevers (Arrow-TL1; NanoWorld, Switzerland) were mounted on a JPK Nanowizard Cellhesion 200 (JPK Instruments AG, Germany), which was set up on an x/y-motorized stage of an inverted optical microscope (Axio ObserverA1, Zeiss, UK). Cantilever spring constants were determined via the thermal noise method55 and cantilevers with spring constants between 0.01 and 0.03 N/m selected. Monodisperse polystyrene beads (diameter: 37.28 ± 0.34 µm; microParticles GmbH, Germany) were glued to the cantilevers as probes56,57.

Xenopus embryos were anesthetized and one hemisphere of the intact brain exposed by removing skin and dura as described in Chien *et al.*51 (**Fig. 2a**). Embryos were then transferred to a Petri dish on the motorized stage and immobilized using a harp slice grid (ALA Scientific, NY, USA). Epifluorescence and brightfield images were taken to identify the OT. On the exposed brains, the region containing the OT was selected. Images of the upper right and lower left corners of the selected region were taken with a CCD camera (Imaging Source, UK) mounted on a TopViewOpticsTM upright imaging system (JPK Instruments AG, Germany) to identify the region of the brain mapped by the AFM. Force–distance curves (maximum indentation force: 7 nN, approach speed: 10 µm/s, data rate: 1,000 Hz) were taken every 20 or 25 µm apart in a raster scan using a custom-written script.

For local brain stiffening experiments, anaesthetized stage 35/36 *Xenopus* embryos with one brain hemisphere exposed as described above were transferred to 1.3× MR solution (composition: 1.3× MBS with 0.04% (w/v) MS222 and 1× P/S/F (pH 7.4); the higher osmolarity retards skin regrowth for the duration of

the experiment). Epifluorescence and brightfield images were collected using a modified AxioZoom V.16 system (Zeiss, UK) connected to an Andor Zyla 4.2 CMOS camera to identify the position of the OT. To induce local strain stiffening at the mid-diencephalon, tipless silicon cantilevers (Shocon-TL; AppNano, CA, USA) with attached polystyrene beads of 89.3 μm diameter (microParticles GmbH, Germany) were used to apply a constant force of 30 nN to a region toward the front of the advancing OT. The force was applied for ~6 h at 25 °C until embryos had reached stage ~39. Controls were treated in the same way except for the AFM application. After removal of the cantilever, manipulated and control embryos were fixed in 4% PFA, and the optic tract labeled with DiI as described above for analysis.

Data analysis. *Image preprocessing of in vitro experiments.* Images of *Xenopus* eye primordia were imported into ImageJ. Some images were corrected for uneven background illumination using a Fourier bandpass filter. Large features in the background were manually removed and images binarized. The resulting binary images were used as input for two independent analyses, Sholl analysis and turning angle analysis (see below). For the turning angle analysis, the region corresponding to the eye primordium was manually adjusted by an ellipse in each image. All the pixels inside this ellipse were set to zero (background), as well as those pixels belonging to connected components smaller than 45 pixels (18.8 μm2). Each eye primordium's center of mass was set as the origin of a 2D coordinate system with the gradient orientated along the *y*-axis.

*Sholl analysis*58. Images were analyzed using the Sholl Analysis plugin in ImageJ. An ellipse was fit to the eye primordium and the initial radius set to $r_i = \sqrt{A/\pi}$, where A is the area of the ellipse. The outer radius was set beyond the extent of the longest axon bundle, and the radius step size (spacing between consecutive circles) was set to 6.25 μm (10 pixels).

In vitro time-lapse experiments. We imported 8-bit greyscale images into Fiji software. Twenty axons per eyeball were chosen at random and the path each growth cone, traversed over a ~3 h period, was manually tracked using the 'Tracking' function in Fiji. After tracking growth cones of 60 axons on both stiff and soft substrates, we analyzed the trajectories using a custom written Matlab script (Mathworks, MA, USA). The growth velocity for each axon *v*growth was calculated by

$$v_{Growth} = \frac{|\vec{p}_s - \vec{p}_e|}{t}$$

with the vector to the start position $\vec{p}_s$ and end position $\vec{p}_e$ of the growth cone and the time t. The speed for each growth cone v_{GC} was calculated by

$$v_{GC} = \frac{\sum_{i=2}^{N} |\vec{p}_i - \vec{p}_{i-1}|}{t}$$

with the position of the growth cone on the *i*th frame $\vec{p}_i$, and the total frame number N. The directionality of the growth cones' path *D* was calculated by

$$D = \frac{v_{Growth}}{v_{GC}}$$

D = 1 corresponds to straight growth, while D close to 0 corresponds to a random walk.

The direction of growth cone migration φ_i for the position $i \in \{x | x \epsilon \mathbb{N};\ x > 64;\ x \leq N\}$ was calculated as follows.

When the third component of $(\vec{p}_i - \vec{p}_{i-4}) \times (\vec{p}_{i-4} - \vec{p}_{i-64})$ being ≥ 0 by

$$\varphi_i = \cos^{-1} \frac{(\vec{p}_i - \vec{p}_{i-4}) \cdot (\vec{p}_{i-4} - \vec{p}_{i-64})}{|\vec{p}_i - \vec{p}_{i-4}| \cdot |\vec{p}_{i-4} - \vec{p}_{i-64}|}$$

When the third component of $(\vec{p}_i - \vec{p}_{i-4}) \times (\vec{p}_{i-4} - \vec{p}_{i-64})$ being < 0, it was calculated as

$$\varphi_i = 2\pi - \cos^{-1} \frac{(\vec{p}_i - \vec{p}_{i-4}) \cdot (\vec{p}_{i-4} - \vec{p}_{i-64})}{|\vec{p}_i - \vec{p}_{i-4}| \cdot |\vec{p}_{i-4} - \vec{p}_{i-64}|}$$

Analysis of axon orientation on plain substrates. Images of axons stained for β-tubulin were imported into Fiji and cropped to regions approximately 140 × 45 μm2. These were analyzed using the OrientationJ plugin. Orientation values were weighted by coherency (a parameter between 0 and 1, which indicates how locally co-aligned image features are). The distribution of angles for each image was adjusted so that the median angle was 0°.

AFM data. To quantify data from *in vivo* AFM indentation experiments, we used a custom-written automated routine based in Matlab to analyze force-distance curves18. This routine is based on the Hertz model59:

$$F = \frac{4}{3} \frac{E}{1 - \nu^2} r^{1/2} \delta^{3/2} = \frac{4}{3} K r^{1/2} \delta^{3/2}$$

with applied force F, Young's modulus E, Poisson's ratio ν, indenter radius r, indentation depth δ, and apparent reduced elastic modulus $K = E/(1 - \nu 2)$. Curves were analyzed for defined indentation depths (**Supplementary Fig. 3**) or the maximum applied force F = 7 nN (**Figs. 2** and **4**). K values were then color-coded and mapped onto the image of the *Xenopus* brain using a custom-written Matlab script (the 'stiffness map').

For the quantification of the mechanical properties of different regions of interest (ROIs), we defined the OT by manually drawing an outline as indicated in **Supplementary Figure 3b**,**d**. Rostral and caudal to the OT (**Fig. 2h**) was defined as an approximately 50-μm wide area rostral and caudal to the tract, respectively, while for the quantification of local gradients parallel to the OT (**Fig. 3b**,**c**), ROIs were defined as described in the text and shown in **Figure 3a**. The front of the OT was defined as an approximately 50-μm wide area in front of the tract, which was ~25 μm wider than the OT on each side, as indicated in **Figure 4a**. The tectum was defined based on its anatomic location (cf. **Figs. 2** and **4**). ROIs were selected three times by hand using a custom-written Matlab script; a pixel was chosen to be part of the ROI if it was selected at least two out of three times. Afterwards, the image of the *Xenopus* brain was scaled down to match the resolution of the stiffness map. Element-wise multiplication of the stiffness map matrix with the downscaled selection matrix

resulted in the selection of the measurements in the selected area. Subsequently, all selected measurements of all experiments were pooled and then further analyzed as described in the statistics section.

Cell density measurements. Image stacks were imported into Fiji. For each brain, the image where the OT was in focus at the caudal bend was determined, and a maximum projection was made of that image and one image before and after it (2 µm *z*-stack height). A Gaussian blur filter (sigma = 2.0) was used to remove noise. The resulting image was thresholded; thresholds were manually adjusted to ensure that most of the nuclei were captured. Regions of interest were selected manually at the rostral and caudal sides of the OT. The image was binarized and the 'Analyze Particle' function (size: 2–ŝ; circularity: 0.5–1.00) was used to acquire the area of nuclei in each ROI. The relative cell density was calculated by dividing the area with nuclei by the total area of the ROI.

OT curvature. To extract the relationship between the local stiffness gradient *M* perpendicular to the OT and the curvature of the OT at each position, we used the following algorithm. The path of the center of the OT was drawn by hand. Every 5th point of this line was selected and data was smoothed to reduce irregularities in the outline (points were approximately 40 µm apart). The curvature *C* at the *i*th selected point was calculated by:

$$C = \frac{1}{R} = \frac{4 \cdot A}{a \cdot b \cdot c}$$

with the radius *R* (which can be negative or positive, depending on *A*) of the circumscribed circle of the triangle between points (*i* − 1), *i* and (*i* + *1*), the 'area' *A* being the third component of ☐☐*ac*×, the three-dimensional (3D) vector ☐*a* which points from (*i* − 1) to *i* (third component of ☐*a* being 0), the 3D vector ☐*c* which points from (*i* − 1) to(*i* + 1) (third component of ☐*c* being 0), the length *aa*=☐, the length *b* of the line between points *i* and (*i* + 1) and the length *cc*=☐. To calculate the corresponding local stiffness gradient perpendicular to the tract *M*, we first fitted a line through five points to obtain the general direction around the middle point, for which we had already calculated the curvature. Thereafter, we calculated the average of the apparent reduced elastic modulus of a 100 × 100 µm2 area left (*K*1) and right (*K*2) of this line (**Fig. 3a**). The gradient was then calculated by:

$$M = \frac{K_1 - K_2}{100\mu m}$$

For better visualization of axon turning toward softer vs. stiffer tissue, the left side of the coordinate system showing local curvature *C* as a function of local stiffness gradient $M < 0$ was rotated by 180° (**Fig. 3b**).

In vitro turning angle analysis. To detect the number of segments of axons in each half of the coordinate system ($x < 0$ and $x > 0$; see "Image preprocessing of *in vitro* experiments" above) that were aligned along the direction defined by the turning angle τ, binary images were rotated by this angle and searched for peaks higher than 20 pixels (~13 µm) in the histogram of the rotated *x*-coordinate. Because the pixels that contribute to the same bin of the histogram may not belong to the same segment of axon in the binary image, we performed an additional connectivity analysis to identify how many segments contribute to each bin. This way, on average ~2,800 axon segments were analyzed per eye primordium. To account for the clockwise growth of axons on 2D substrates60, turning angles were normalized by subtracting the median angle of the total explant from the median angle of the individual halves. The distribution of median turning angles for

both image halves were plotted in **Figure 3e**; for better visualization of turning toward softer vs. stiffer substrates, the left side of the coordinate system ($x < 0$) was rotated by 180° and data points were pooled.

In a second approach, we used time-lapse imaging of individual axons or tight axon bundles grown on substrates incorporating a linear stiffness gradient. The initial direction of the axon was determined by the most recent ~50 μm of axon growth, and only straight axons growing approximately perpendicular to the stiffness gradient were selected. Axons were left to grow for 1 h, and the new growth direction determined by determining the angle between the initial growth direction and the new axon segment (**Fig. 3f**). To correct for the clockwise growth of axons in 2D cultures60, equal numbers of axons were selected from each side of the stiffness gradient.

Shape characterization of the OT. Outlines of the OT distal of the optic chiasm were drawn manually in Corel Draw X5. The elongation of the OT was calculated by the major-to-minor axis ratio using an automated algorithm in Matlab as previously described24. Briefly, the axes were determined by fitting ellipses—with the same normalized second central moment as the OT area—around OTs.

Statistics and visualization. Data were collected from at least 3 independent experiments ($N \geq 3$). Sample sizes were chosen using a Power & Sample Size Calculator (http://www.statisticalsolutions.net/pssZtest_calc.php). The order of data collection was randomized; no blinding was done and no data were excluded from the analysis. Normality was tested for all data sets using the Shapiro-Wilk test; variances were compared using a $\chi 2$ test. In case of normal distribution, statistical comparisons between two groups were done using two-tailed unpaired or paired *t*-tests, and between more than two groups using ANOVA. If data did not follow a Gaussian distribution, Kruskal-Wallis ANOVA, Mann-Whitney, and one-sample Wilcoxon signed-rank tests were used to statistically compare more than two groups, only two groups, or data within one group, respectively. Data were plotted as box plots, with boxes showing the 25th, 50th (median), and 75th percentiles; whiskers show the spread of the data (excluding outliers), and an 'O' shows the mean score for a group. A **Supplementary Methods** C**hecklist** is available.

Data availability. The data that support the findings of this study, as well as the custom Matlab codes used in the analyses, are available from the corresponding author upon reasonable request.